

# Noisy MRI Reconstruction via MAP Estimation with an Implicit Deep-Denoiser Prior

Nikola Janjušević<sup>1</sup>, Amirhossein Khalilian-Gourtani<sup>2</sup>, Yao Wang<sup>3</sup>, Li Feng<sup>1</sup>,

**Abstract**—Accelerating magnetic resonance imaging (MRI) remains challenging, particularly under realistic acquisition noise. While diffusion models have recently shown promise for reconstructing undersampled MRI data, many approaches lack an explicit link to the underlying MRI physics, and their parameters are sensitive to measurement noise, limiting their reliability in practice. We introduce *Implicit-MAP (ImMAP)*, a diffusion-based reconstruction framework that integrates the acquisition noise model directly into a maximum a posteriori (MAP) formulation. Specifically, we build on the stochastic ascent method of Kadkhodaie et al. and generalize it to handle MRI encoding operators and realistic measurement noise. Across both simulated and real noisy datasets, ImMAP consistently outperforms state-of-the-art deep learning (LPDSNet) and diffusion-based (DDS) methods. By clarifying the practical behavior and limitations of diffusion models under realistic noise conditions, ImMAP establishes a more reliable and interpretable baseline for diffusion-based accelerated MRI reconstruction.

**Index Terms**—Denoising diffusion generative model, inverse problems, deep-learning, denoising, MRI

## I. INTRODUCTION AND BACKGROUND

Magnetic resonance imaging (MRI) is a widely used, non-invasive technique for the clinical diagnosis of conditions affecting many organs. However, a primary limitation of MRI is its slow acquisition speed, which is constrained by fundamental physical principles. To accelerate scanning, parallel imaging methods use multiple receiver coils to acquire undersampled k-space data, thereby reducing scan time and performing a regularized reconstruction at inference [1]. This regularization is traditionally guided by hand-crafted priors, however, recently end-to-end trained deep neural networks have shown state-of-the-art performance [2].

Another growing body of related literature is zero-shot deep denoising diffusion generative models (DDGMs) [3]–[8]. These models have emerged as a powerful class of methods for solving image inverse problems. In natural image domains, these models have demonstrated an exceptional ability to produce realistic and high-fidelity reconstructions. Fundamentally, diffusion models are trained to learn the score function, i.e. the gradient of the log-probability of the data distribution, through a denoising process that gradually removes noise from corrupted samples. By reversing this diffusion process, the models can generate samples from the learned data distribution and effectively recover images from incomplete or degraded measurements [6]. In MRI, diffusion-based approaches have

shown promising results in achieving high acceleration rates under simulated noise conditions [4]. However, DDGMs are typically formulated using stochastic differential equations or Markov chains, both of which are decoupled from the underlying MRI physics and the applicability of DDGMs to real-world MRI data with measurement noise introduced by the scanner remains largely unexplored.

In a series of recent publications [9]–[11], we have introduced a framework for the interpretable design of deep denoisers that generalize effectively across, and even beyond, their training noise levels has been introduced. We further extended this framework to the problem of MRI reconstruction, demonstrating its applicability in both supervised and self-supervised learning settings [2]. In this work, we expand these ideas to diffusion-based models and propose an interpretable construction framework for diffusion models tailored to MRI reconstruction. Specifically, we expand upon the formulation of diffusion models introduced in Kadkhodaie et al. [12] to address inverse problems in the presence of observation noise. We show state-of-the-art performance of the proposed approach on both synthetically added noise and real MRI acquisitions with scanner noise.

### A. MRI Reconstruction Problem

We model our observations as an undersampled multicoil Fourier domain signal  $\mathbf{y} \in \mathbb{C}^{N_s C}$ , with  $C$  coils, of a ground-truth image  $\mathbf{x} \in \mathbb{C}^N$ , with Fourier sampling locations denoted by index-set  $\Omega$  and coil-sensitivity maps  $\mathbf{s} \in \mathbb{C}^{NC}$ ,

$$\mathbf{y}_c = \mathbf{I}_\Omega \mathbf{F}(\mathbf{s}_c \circ \mathbf{x}) + \boldsymbol{\nu}_c, \quad \forall c = 1, \dots, C, \quad (1)$$

where  $\mathbf{F}$  is the  $N$ -pixel 2D-DFT matrix,  $\mathbf{s}_c \in \mathbb{C}^N \forall c$ ,  $\circ$  denotes element-wise multiplication, and  $\mathbf{I}_\Omega \in \{0, 1\}^{N_s \times N}$  is the row-removed identity matrix with kept rows indicated by  $\Omega$ . We consider our observations to be noise-whitened such that  $\boldsymbol{\nu}[n] \sim \mathcal{N}(0, \boldsymbol{\Sigma}_y)$  is Gaussian noise with noise-covariance matrix  $\boldsymbol{\Sigma}_y \in \mathbb{C}^{C \times C}$  identically distributed for all pixels  $n \in [1, N_s]$ . We denote this observation model through the encoding operator  $\mathbf{A}$  defined such that  $\mathbf{y} = \mathbf{A}\mathbf{x} + \boldsymbol{\nu}$ . We say the observation is accelerated by a factor of  $R = N/N_s$ . For the remainder of this manuscript, we follow the mathematical notation of [1].

### B. Stochastic Ascent with a Denoiser’s Implicit Prior

In this section, we present the stochastic gradient descent algorithm with a denoiser’s implicit prior of Kadkhodaie et al. [12]. Let  $\mathbf{z} = \mathbf{x} + \mathbf{n}$  where  $\mathbf{x} \sim p$  and  $\mathbf{n} \sim g_\sigma = \mathcal{N}(0, \sigma^2 \mathbf{I})$ . Then we may obtain the following relation (Tweedie’s Formula [12]) directly from expressing the noisy

<sup>1</sup>New York University Grossman School of Medicine, {<sup>1</sup>Radiology Department, <sup>2</sup>Neurology Department}, New York, NY 10016, USA.

<sup>3</sup>New York University Tandon School of Engineering, Electrical and Computer Engineering Department, Brooklyn, NY 11201, USA.

Please send all correspondence regarding to this manuscript to N. Janjušević (email:nikola.janjušević@nyulangone.org).

image distribution  $p_\sigma$  as the convolution of the noiseless image distribution  $p$  and the Gaussian PDF  $g_\sigma$ ,

$$p_\sigma(\mathbf{z}) = \int_{\mathbb{R}^N} g_\sigma(\mathbf{z} - \mathbf{x})p(\mathbf{x})d\mathbf{x} \quad (2)$$

$$\sigma^2 \nabla_{\mathbf{z}} \log p_\sigma(\mathbf{z}) = \mathbb{E}[\mathbf{x}|\mathbf{z}] - \mathbf{z}. \quad (3)$$

Now let  $f$  be an MMSE Gaussian-noise denoiser, ex. we trained a learned denoiser  $f = \arg \min_f \mathbb{E}[\|\mathbf{x} - f(\mathbf{z}; \sigma)\|_2^2]$  across a range of noise-levels  $\sigma$ . Then  $f(\mathbf{z}; \sigma) \approx \mathbb{E}[\mathbf{x}|\mathbf{z}]$  and we have approximate access to the gradient of the log-probability of the noisy image distribution,

$$\sigma^2 \nabla_{\mathbf{z}} \log p_\sigma(\mathbf{z}) = \mathbb{E}[\mathbf{x}|\mathbf{z}] - \mathbf{z} \approx f(\mathbf{z}; \sigma) - \mathbf{z}. \quad (4)$$

Tweedie's formula (4) tells us that the MMSE estimate of the ground-truth  $\mathbf{x}$  given a noisy  $\mathbf{z}$  is achieved by a single gradient ascent step on the log-probability of  $p_\sigma$ ,  $\mathbb{E}[\mathbf{x}|\mathbf{z}] = \mathbf{z} + \sigma^2 \nabla_{\mathbf{z}} \log p_\sigma(\mathbf{z})$  with step-size  $\sigma^2$ . However,  $p_\sigma$  is only a Gaussian-blurred version of our true image distribution  $p$ . *The key-insight of Kadkhodaie et al. [12] is that we may interpret the score function of the noisy distribution,  $\sigma^2 \nabla_{\mathbf{z}} \log p_\sigma(\mathbf{z})$ , as an approximate ascent direction on the true image distribution.* If we take a fractional step in this direction, our new estimate will be closer to the true image distribution, less noisy ( $\sigma \downarrow$ ), and we will have access to an even more accurate ascent direction w.r.t. the true image distribution. Upon this insight, Kadkhodaie et al. [12] propose the following algorithm, which may be interpreted as a coarse-to-fine gradient ascent on the log-probability,

$$\mathbf{z}_{t+1} = \mathbf{z}_t + h_t(f(\mathbf{z}_t) - \mathbf{z}_t) + \epsilon_t, \quad (5)$$

with starting point  $\mathbf{z}_0 \sim \mathcal{N}(0, \mathbf{I})$ , step-size  $h_t \in [0, 1]$  and stochastic noise term  $\epsilon_t \sim \mathcal{N}(0, \gamma_t^2 \mathbf{I})$  introduced to help escape local maxima. In the same work, Kadkhodaie et al. [12] extended their algorithm to handle conditioning on measurement data,  $\mathbf{y} = \mathbf{A}\mathbf{x}$ , by performing maximization of the log-posterior using Baye's rule, i.e.,  $\arg \max_{\mathbf{x}} \log p(\mathbf{x}|\mathbf{y}) = \arg \max_{\mathbf{x}} \log p(\mathbf{x}) + \log p(\mathbf{y}|\mathbf{x})$ . However, their method relied on  $\mathbf{y}$  being noise-free and having an easily SVD decomposable observation operator  $\mathbf{A}$ , limiting its direct application to large-scale MR imaging inverse-problems.

In light of these limitations, in Section II we propose an extension of Kadkhodaie's measurement-conditioned stochastic ascent algorithm which accounts for measurement noise and the large-scale nature of the MRI encoding operator.

## II. PROPOSED METHOD

### A. The Implicit MAP Algorithm

Let  $\mathbf{y} = \mathbf{A}\mathbf{x} + \nu$  where  $\nu \sim \mathcal{N}(0, \Sigma_y)$ . We seek the to reconstruct  $\mathbf{x}$  from  $\mathbf{y}$  via obtaining a MAP estimate,

$$\mathbf{x}^\diamond = \arg \max_{\mathbf{x}} p(\mathbf{x}|\mathbf{y}) \quad (6)$$

$$= \arg \max_{\mathbf{x}} \log p(\mathbf{x}) + \log p(\mathbf{y}|\mathbf{x}). \quad (7)$$

We tackle this problem with a coarse-to-fine stochastic gradient ascent on the log-prior and log-likelihood functions,

$$\mathbf{z}_{t+1} = \mathbf{z}_t + h_t \sigma_t^2 (\nabla_{\mathbf{z}_t} \log p_{\sigma_t}(\mathbf{z}_t) + \nabla_{\mathbf{z}_t} \log p(\mathbf{y}|\mathbf{z}_t)) + \epsilon_t, \quad (8)$$

using the prior implicitly encoded by a trained denoiser  $f$  to access the prior score function via Tweedie's formula (4). We switch to the notation to variable  $\mathbf{z}$  to indicate that our intermediate variables  $\mathbf{z}_t$  belong to the noisy image distribution,  $\mathbf{z}_t \sim p_{\sigma_t}$ . To access the likelihood score-function,  $\nabla_{\mathbf{z}_t} \log p(\mathbf{y}|\mathbf{z}_t)$ , we model  $\mathbf{z}_t$  as a noisy version of our desired ground-truth signal,  $\mathbf{z}_t \sim \mathcal{N}(\mathbf{x}, \sigma_t^2 \mathbf{I})$ . Following [6], [8], we approximate the distribution of a denoised  $\mathbf{z}_t$ , i.e.  $f(\mathbf{z}_t)$ , with a Gaussian distribution (i.e. a Laplace Approximation),

$$f(\mathbf{z}_t) \sim \mathcal{N}(\mathbb{E}[\mathbf{x}|\mathbf{z}_t], \mathbf{V}_t),$$

where the variance-matrix  $\mathbf{V}_t$  is a modeling parameter which we set to  $\mathbf{V}_t = \frac{\sigma_t^2}{1+\sigma_t^2} \mathbf{I}$  in practice, following [8]. We derive the likelihood function as,

$$p(\mathbf{y}|\mathbf{z}_t) = \mathcal{N}(\mathbf{y} | \mathbf{A} \mathbb{E}[\mathbf{x}|\mathbf{z}_t], \Sigma_t),$$

where  $\Sigma_t = \Sigma_y + \mathbf{A}\mathbf{V}_t\mathbf{A}^H$ . Taking the gradient of the log-likelihood yields,

$$\begin{aligned} \nabla_{\mathbf{z}_t} \log p(\mathbf{y}|\mathbf{z}_t) &= -\nabla_{\mathbf{z}_t} \frac{1}{2} \|\Sigma_t^{-1/2} (\mathbf{A} \mathbb{E}[\mathbf{x}|\mathbf{z}_t] - \mathbf{y})\|_2^2 \\ &= -\nabla_{\mathbf{z}_t} \mathbb{E}[\mathbf{x}|\mathbf{z}_t]^H \mathbf{A}^H \Sigma_t^{-1} (\mathbf{A} \mathbb{E}[\mathbf{x}|\mathbf{z}_t] - \mathbf{y}). \end{aligned} \quad (9)$$

With  $\mathbb{E}[\mathbf{x}|\mathbf{z}_t] \approx f(\mathbf{z}_t)$ , we implement  $\nabla_{\mathbf{z}_t} \mathbb{E}[\mathbf{x}|\mathbf{z}_t]^H \mathbf{v} \approx \mathbf{J}_t^H \mathbf{v}$  with a vector-jacobian product (VJP) with respect to our trained denoiser  $f^1$ . This allows us to solve the symmetric linear system in the likelihood term (9) via the conjugate gradient method [8]. Lastly, we employ a stochastic noise term ( $\epsilon_t$ ) with stochasticity term  $\beta \in (0, 1]$  for purposes of escaping local minima, achieving the stochastic MAP estimation algorithm with implicit denoiser prior (ImMAP), shown in Algorithm 1.

### B. Comparison of ImMAP to Other Diffusion-based Methods

Denosing diffusion generative models (DDGMs) are formulated by modeling the gradual transition of a noise-free image distribution  $p_0$  into a distribution of pure noise  $p_T$ , either through a Markov-chain process or more generally as a continuous time stochastic differential equation with forward (corruption) process,

$$d\mathbf{x}_t = h(\mathbf{x}_t, t)dt + l(t)d\mathbf{W}_t, \quad (10)$$

with  $\mathbf{x}_0 \sim p_0$  and  $\mathbf{W}_t$  denoting a Wiener process. Solving (10) backwards in time is then interpreted as obtaining a sample from the noise-free image distribution  $p_0$ , for appropriately chosen  $h$  and  $l$  [6]. These equations can be easily extended to sampling from a conditional distribution  $p_0(\mathbf{x}|\mathbf{y})$  given measurements  $\mathbf{y}$  [6].

This formulation of DDGMs introduces a plethora of modeling choices/assumptions having solely to do with the SDE/Markov process, unrelated to any imaging inverse problem. In contrast, the derivation of ImMAP makes no such

<sup>1</sup>The VJP operator is accessible via standard automatic differentiation libraries, often via a pullback function.

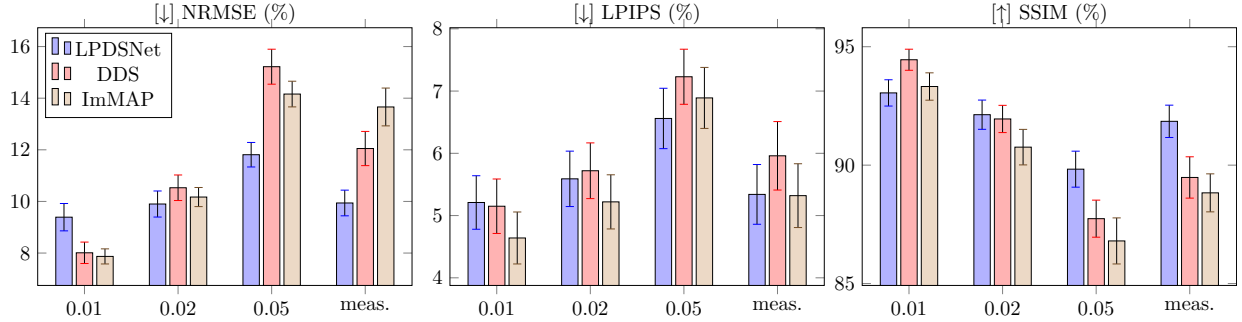


Fig. 1: Quantitative performance of end-to-end (LPDSNet), and denoising diffusion based (DDS, ImMAP) reconstruction methods on the T1w brain test dataset. NRMSE/LPIPS/SSIM (%) shown at  $8\times$  acceleration and across noise-levels ( $\sigma_y$ ). Noise is considered in two scenarios: simulated noise added to the coil-combined fully-sampled image data (i.e.  $(\Sigma_y)_{cc} = \sigma_y \in (0.01, 0.02, 0.05)$ ), and measurement noise (meas.,  $\Sigma_y = \hat{\Sigma}_y$ ) where the original fully-sampled k-space data is retrospectively undersampled. Error bars show standard-error of the mean over 16 test-volumes.

---

**Algorithm 1: ImMAP**


---

**Input:**  $\mathbf{y} \sim \mathcal{CN}(\mathbf{A}\mathbf{x}, \Sigma_y)$ ,  $\Sigma_y$ ,  $\mathbf{A}$ ,  $f$ ,  $\beta = 0.01$ ,  
 $\sigma_L = 0.01$ ,  $h_0 = 0.01$

**Output:**  $\mathbf{x}^\diamond = \arg \max_{\mathbf{x}} \log p(\mathbf{x}) + \log p(\mathbf{y}|\mathbf{x})$

```

1 Draw  $\mathbf{z}_0 \sim \mathcal{CN}(0, \mathbf{I})$ 
2  $t = 1$ ,  $\sigma_t^2 = 1$ 
3 while  $\sigma_t > \sigma_L$  do
  // Denoising step and VJP Operator
4  $\hat{\mathbf{z}}_t, \mathbf{J}_t^H \leftarrow \text{pullback}(f(\cdot, \sigma_t), \mathbf{z}_t)$ 
5  $\sigma_t^2 \leftarrow \|\hat{\mathbf{z}}_t - \mathbf{z}_t\|_2^2 / N$ 
  //  $\Pi$ GDM [8] Laplace Approximation
6  $\Sigma_t \leftarrow \Sigma_y + \frac{\sigma_t^2}{1 + \sigma_t^2} \mathbf{A}\mathbf{A}^H$ 
7  $\mathbf{v}_t \leftarrow \Sigma_t^{-1} (\mathbf{A}\hat{\mathbf{z}}_t - \mathbf{y})$  // solve via cg
8  $\mathbf{u}_t \leftarrow -\mathbf{J}_t^H \mathbf{A}^H \mathbf{v}_t$ 
  // Stochastic Gradient Ascent
9  $h_t \leftarrow h_0 \frac{t}{1 + h_0(t-1)}$ 
10  $\gamma_t^2 \leftarrow \sigma_t^2 ((1 - \beta h_t)^2 - (1 - h_t)^2)$ 
11  $\boldsymbol{\epsilon}_t \sim \mathcal{CN}(0, \gamma_t^2 \mathbf{I})$ 
12  $\mathbf{z}_{t+1} \leftarrow \mathbf{z}_t + h_t (\hat{\mathbf{z}}_t - \mathbf{z}_t + \sigma_t^2 \mathbf{u}_t) + \boldsymbol{\epsilon}_t$ 
13  $t \leftarrow t + 1$ 
14 return  $\mathbf{x}^\diamond = \mathbf{z}_t$ 

```

---

modeling assumptions and instead relies only on Tweedie’s formula (4) [6] and MRI physics.

Recently, Chung et al. proposed Decomposed Diffusion Sampling (DDS) [4], a DDGM designed specifically for large scale noisy inverse problems. DDS is formulated as a Krylov-subspace method, relying on a “few-step” conjugate gradient algorithm to keep its intermediate estimates close to a Krylov-subspace tangent to the noisy image manifold. However, the existence of such a tangent space is not necessarily valid in practice, and their choice of number of conjugate-gradient steps is shown to greatly influence their algorithm’s performance [4]. Additionally, they introduce another hyperparameter  $\gamma$  to control the trade-off between data-consistency and their score-based denoiser, which we find in practice needs tuning for different MRI noise-levels (see Section III-D).

### III. RESULTS

#### A. Dataset and Experimental Settings

The performance of all models was evaluated on an internal MRI brain dataset consisting of fully-sampled T1w multicoil k-space data (i.e.  $\mathbf{y} = \mathbf{F}\mathbf{S}\mathbf{x} + \boldsymbol{\nu}$ ). 66 fully-sampled volumes ( $\sim 60$  slices each) were used for training with 16 used as a held-out test set. This data was used in two experimental settings,

- 1) **simulated noise:** the *fully-sampled coil-combined image* reconstruction ( $\mathbf{x}' = \mathbf{S}^H \mathbf{F}^H \mathbf{y}$ ) is passed through an MRI encoding operator  $\mathbf{A} = \mathbf{I}_\Omega \mathbf{F} \mathbf{S}$ ,

$$\mathbf{y}' = \mathbf{A}\mathbf{x}' + \boldsymbol{\nu}', \quad (11)$$

with noise  $\boldsymbol{\nu}' \sim \mathcal{N}(0, \sigma_y \mathbf{I})$  added in simulation. Reconstruction involves recovering  $\mathbf{x}'$  from k-space  $\mathbf{y}'$ , which contains measurement coil-noise. Quantitative error measurement compares reconstructions  $\hat{\mathbf{x}}$  to  $\mathbf{x}'$  with no irreducible error due to noise. For simulated noise experiments, white Gaussian noise ( $\Sigma_y = \text{diag}(\sigma_y)$ ) was added under three noise-levels,  $\sigma_y \in (0.01, 0.02, 0.05)$ .

- 2) **measurement noise:** the *fully-sampled multi-coil k-space* is retrospectively undersampled,

$$\mathbf{y}' = \mathbf{I}_\Omega \mathbf{y} = \mathbf{I}_\Omega (\mathbf{F}\mathbf{S}\mathbf{x} + \boldsymbol{\nu}) = \mathbf{A}\mathbf{x} + \mathbf{I}_\Omega \boldsymbol{\nu}, \quad (12)$$

with noise  $\boldsymbol{\nu}$  coming directly from the scanner. Reconstruction involves recovering the ground-truth noise-free image  $\mathbf{x}$  from k-space  $\mathbf{y}'$ . Note that  $\mathbf{x}$  does not contain measurement noise and is inaccessible to us (due to the SNR of the collected k-space data). Quantitative error measurement compares reconstructions  $\hat{\mathbf{x}}$  to  $\mathbf{x}'$  with irreducible error due to subsampled measurement noise  $\mathbf{I}_\Omega \boldsymbol{\nu}$ , which is inseparable from the measurement k-space data (and hence inseparable from  $\mathbf{x}'$ ). For measurement noise experiments, estimated coil-noise covariance matrices  $\Sigma_y$  were obtained via a wavelet-filter multicoil image domain method, following [1]. We denote experiments in the measurement noise setting as “ $\sigma_y = \text{meas.}$ ” for notational brevity.

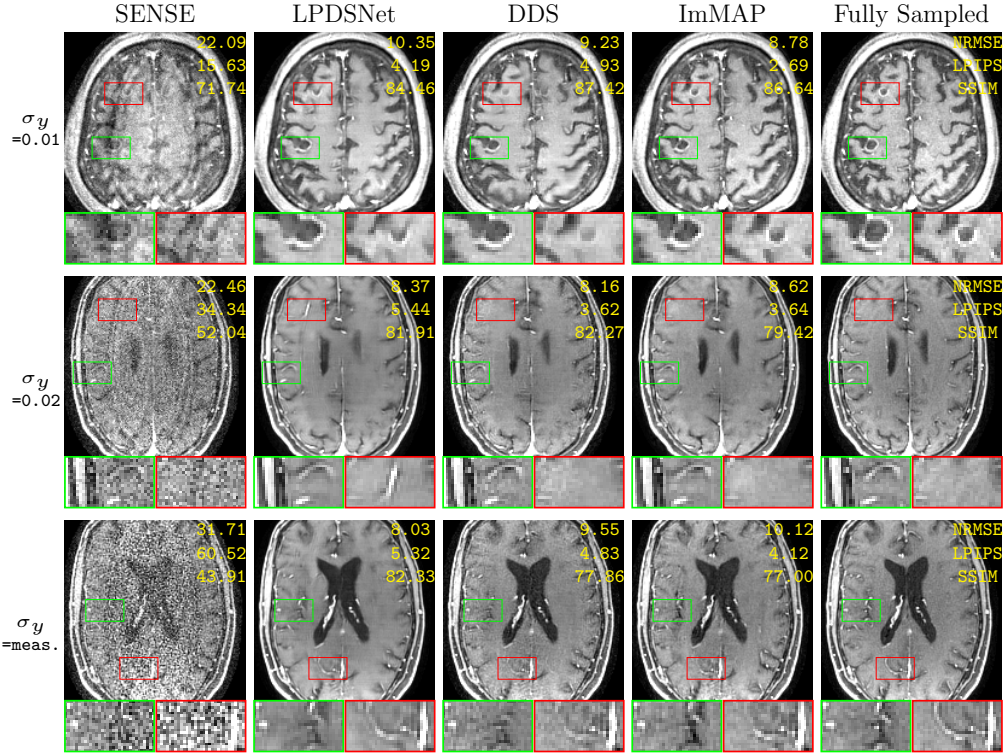


Fig. 2: Visual comparison of ImMAP joint denoising and reconstruction MRI at  $8\times$  acceleration against classical reconstruction (SENSE [13]), end-to-end deep reconstruction (LPDSNet [2]), denoising diffusion model (DDS [4]), across noise-levels ( $\sigma_y$ ). Quantitative metrics (NRMSE/LPIPS/SSIM (%)) are shown in yellow above each reconstruction.

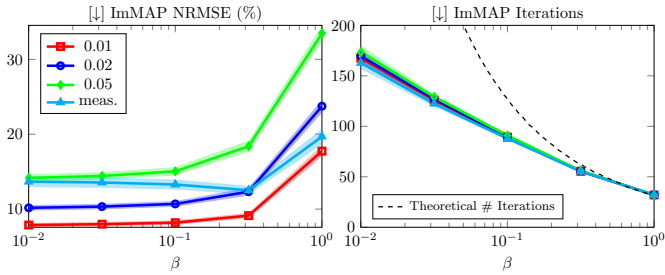


Fig. 3: Ablation of ImMAP’s noise-injection parameter  $\beta \in (0, 1]$ . **Left:** average NRMSE over the T1w brain test set vs.  $\beta$ , across noise-levels  $\sigma_y = (0.01, 0.02, 0.05, \text{meas.})$ . Standard error of the mean shown via shaded regions. **Right:** Corresponding average number of iterations vs.  $\beta$ , across noise-levels.

For all experiments,  $8\times$  Cartesian subsampling was used in a single readout direction with a 4% wide region of k-space included. Coil sensitivity maps were obtained by the ESPIRiT algorithm [13] applied to the center of k-space.

### B. Training and Implementation

We trained a single noise-adaptive denoiser  $f$  (using the LPDSNet architecture [2] with  $A = I$ ) on fully-sampled reconstructions of the T1w brain data with synthetic additive Gaussian white noise (AWGN) in the range  $\sigma_t \in [0, 0.5]$ . This denoiser was used for both the ImMAP and DDS based

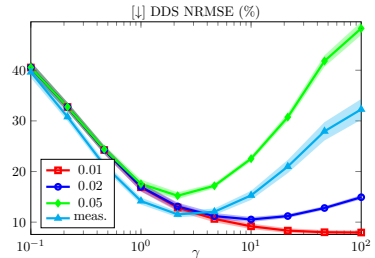


Fig. 4: DDS performance (average volume NRMSE) on  $8\times$  accelerated T1w brain test-set with varying  $\gamma$  hyperparameter over different noise levels  $\sigma_y = (0.01, 0.02, 0.05, \text{meas.})$ . Standard error of the mean shown via shaded regions. DDS takes 83 iterations.

inferences for fair comparison. We trained two noise-adaptive end-to-end reconstruction networks (LPDSNet [2]) on  $8\times$  accelerated simulated noise data and measurement noise data. Both the denoising LPDSNet (used by ImMAP and DDS) and reconstruction LPDSNet shared the same architecture hyperparameters for fair comparison (30 layers, 169 channels, and  $7 \times 7$  conv. kernels). Hyperparameters of DDS [4] were set as  $M = 5$ ,  $\eta = 0.8$ , 83 iterations, and  $\gamma$  set by performing a grid-search per noise-level (see Section III-D).

### C. Joint Reconstruction and Denoising Performance

Fig.1 shows the quantitative performance of ImMAP against the end-to-end reconstruction network LPDSNet [2]

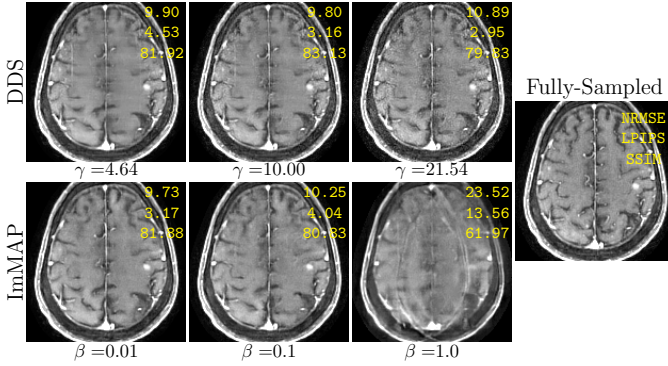


Fig. 5: Visualization of  $8\times$  reconstruction at  $\sigma_y = 0.02$  when changing hyperparameters for DDS ( $\gamma$ ) and ImMAP ( $\beta$ ) on a slice from the T1w brain test-set. NRMSE/LPIPS/SSIM (%) shown on each image as compared to the fully-sampled reconstruction.

(competitive with E2EVarNet [14]) and the state-of-the-art denoising diffusion model DDS [4]. Performance was measured across three metrics: Normalized Root-Mean-Squared-Error ( $\downarrow$  NRMSE), Learned Perceptual Image Patch Similarity (LPIPS) [15] ( $\downarrow$  LPIPS), and the Structural Similarity Image Metric [16] ( $\uparrow$  SSIM). Across all metrics, ImMAP performs competitively with DDS. ImMAP is favored by LPIPS over DDS, especially in the low-noise range ( $\sigma_y = 0.01$ ). The performance on measurement noise the setting ( $\sigma_y = \text{meas.}$ ) heavily favors the end-to-end reconstruction of LPDSNet, likely due to the oversmoothing tendencies of end-to-end networks [4] being favored by the presence of the irreducible noise term in image quality metric computations.

Fig. 2 shows representative visual examples from each reconstruction method across noise-levels, with addition of the classical reconstruction baseline method SENSE [13]. Quantitative metrics are included for each reconstruction. We observe that ImMAP has very strong low-noise ( $\sigma_y = 0.01$ ) performance, recovering lesions missed/obscured by SENSE, LPDSNet, and DDS (see image zooms). For the visual on  $\sigma_y = 0.02$ , we observe competitive performance across all quantitative metrics, however, visual inspection reveals a stark difference. LPDSNet is shown to fail to remove aliasing artifacts and DDS is shown to produce noise-like artifacts around the brain edges, while ImMAP achieves superior visual quality. For  $\sigma_y = \text{meas.}$ , we observe that ImMAP is able to recover fine texture and details while LPDSNet appears to oversmooth image regions and DDS appears again to introduce noise-like artifacts.

#### D. Ablation of ImMAP and DDS

The proposed ImMAP demonstrates strong reconstruction stability w.r.t. its noise-injection/stochasticity parameter ( $\beta$ ), where  $\beta \rightarrow 0$  achieves maximum noise-injection and  $\beta = 1$  removes noise-injection. As noise injection is introduced to help escape local-maxima, we expect this parameter to improve reconstruction performance as  $\beta \rightarrow 0$ . Additionally,  $\beta$  implicitly defines a noise-schedule for  $\sigma_t$ , and hence the number of iterations of ImMAP until convergence. This schedule

is not followed strictly due to the noise-level estimation of ImMAP (see Line 5 of Alg.1). Fig. 3 plots the quantitative reconstruction performance and iteration count of ImMAP with varying  $\beta$ . We see that, across noise-levels, performance of ImMAP improves as  $\beta \rightarrow 0$ , with similar reconstruction performance for a large range of values until  $\beta > 0.3$ . This is with the exception of reconstruction in the measurement noise setting, where irreducible measurement noise is likely favoring a reconstruction with less fidelity at high  $\beta$ . As  $\beta$  increases, we also see that the algorithm takes fewer iterations to converge. As in Kadkhodaie et al. [12], we find that the number of iterations until convergence is much lower than theoretically determined by the  $\beta$ -defined noise-schedule of  $\sigma_t$ . It is clear that  $\beta > 0$  should be set as low as possible (0.01 is sufficient), taking into account any possible computational budget.

State-of-the-art diffusion model DDS [4] has its own hyperparameters, of which  $\gamma$ , corresponding to a Lagrange multiplier term in its conjugate gradient solves, requires careful tuning. Fig. 4 shows the performance of DDS (NRMSE) vs.  $\gamma$ , across noise-levels. We observe that the optimal point (minimum) of each noise-level curve occurs in a different location. In Section III-C, we used the optimal  $\gamma$  determined from these curves. In practice, despite fully-sampled reference data being used for training, fully-sampled reference data at the desired inference noise-level may not be available, making this grid-search for  $\gamma$  difficult or uninformative. In contrast, the optimal choice of hyperparameter ( $\beta$ ) for ImMAP is much clearer.

Fig. 5 shows a visual comparison of hyperparameter changes for both DDS and the proposed ImMAP. DDS shows smoothing and artifact introduction with decreasing  $\gamma$ . Additionally, the optimal setting of  $\gamma$  on this example reconstruction is conflicting between image metrics. In contrast, ImMAP shows similar visual quality for both  $\beta = 0.01$  and  $\beta = 0.1$ , with better quantitative performance across all metrics at lower  $\beta$ .

## IV. CONCLUSION

We introduced ImMAP, a diffusion-based MRI reconstruction method that integrates acquisition physics directly into a MAP estimation framework. Experiments on both simulated noise and measurement noise reconstruction tasks demonstrate that ImMAP outperforms state-of-the-art deep learning and diffusion-based approaches, preserving anatomical detail without noise amplification or oversmoothing. Notably, it achieves robust performance without the parameter tuning/sensitivity of existing diffusion methods. Together, these results establish ImMAP as a reliable and interpretable baseline, clarifying the practical utility and limitations of diffusion models for accelerated MRI reconstruction.

## ACKNOWLEDGMENTS

This work was supported in part by the NIH (R01EB030549, EB031083, R21EB032917, and P41EB017183) and was performed under the rubric of the Center for Advanced Imaging Innovation and Research (CAI2R), an NIBIB National Center for Biomedical Imaging and Bioengineering.

## REFERENCES

- [1] N. Janjušević, J. Chen *et al.*, “Self-supervised noise adaptive mri denoising via repetition to repetition (rep2rep) learning,” *Magnetic Resonance in Medicine*, Nov. 2025. [Online]. Available: <http://dx.doi.org/10.1002/mrm.70155>
- [2] N. Janjušević, A. Khalilian-Gourtani *et al.*, “Learned primal dual splitting for self-supervised noise-adaptive mri reconstruction,” in *2025 IEEE 22nd International Symposium on Biomedical Imaging (ISBI)*, 2025, pp. 1–4.
- [3] Y. Zhu, K. Zhang *et al.*, “Denoising diffusion models for plug-and-play image restoration,” in *Proceedings of the IEEE/CVF conference on computer vision and pattern recognition*, 2023, pp. 1219–1229.
- [4] H. Chung, S. Lee, and J. C. Ye, “Decomposed diffusion sampler for accelerating large-scale inverse problems,” in *12th International Conference on Learning Representations, ICLR 2024*, 2024.
- [5] J. Ho, A. Jain, and P. Abbeel, “Denoising Diffusion Probabilistic Models,” in *Advances in Neural Information Processing Systems*, vol. 33. Curran Associates, Inc., 2020, pp. 6840–6851.
- [6] G. Daras, H. Chung *et al.*, “A survey on diffusion models for inverse problems,” *arXiv preprint arXiv:2410.00083*, 2024.
- [7] F. Rozet, G. Andry *et al.*, “Learning diffusion priors from observations by expectation maximization,” in *The Thirty-eighth Annual Conference on Neural Information Processing Systems*, 2024.
- [8] J. Song, A. Vahdat *et al.*, “Pseudoinverse-guided diffusion models for inverse problems,” in *International Conference on Learning Representations*, 2023.
- [9] N. Janjušević, A. Khalilian-Gourtani, and Y. Wang, “CDLNet: Noise-Adaptive Convolutional Dictionary Learning Network for Blind Denoising and Demosaicing,” *IEEE Open Journal of Signal Processing*, vol. 3, pp. 196–211, 2022.
- [10] —, “Gabor is enough: Interpretable deep denoising with a gabor synthesis dictionary prior,” in *2022 IEEE 14th Image, Video, and Multidimensional Signal Processing Workshop (IVMSP)*, 2022, pp. 1–5.
- [11] N. Janjušević, A. Khalilian-Gourtani *et al.*, “GroupCDL: Interpretable denoising and compressed sensing MRI via learned group-sparsity and circulant attention,” *IEEE Transactions on Computational Imaging*, vol. 11, pp. 201–212, 2025.
- [12] Z. Kadhodaie and E. Simoncelli, “Stochastic solutions for linear inverse problems using the prior implicit in a denoiser,” *Advances in Neural Information Processing Systems*, vol. 34, pp. 13 242–13 254, 2021.
- [13] M. Uecker, P. Lai *et al.*, “Espirit—an eigenvalue approach to autocalibrating parallel mri: Where sense meets grappa,” *Magnetic Resonance in Medicine*, vol. 71, no. 3, p. 990–1001, May 2013.
- [14] A. Sriram, J. Zbontar *et al.*, “End-to-end variational networks for accelerated mri reconstruction,” in *Medical Image Computing and Computer Assisted Intervention—MICCAI 2020: 23rd International Conference, Lima, Peru, October 4–8, 2020, Proceedings, Part II 23*. Springer, 2020, pp. 64–73.
- [15] R. Zhang, P. Isola *et al.*, “The unreasonable effectiveness of deep features as a perceptual metric,” in *CVPR*, 2018.
- [16] Z. Wang, A. Bovik *et al.*, “Image quality assessment: from error visibility to structural similarity,” *IEEE Transactions on Image Processing*, vol. 13, no. 4, pp. 600–612, 2004.